# Theoretical predictions of wurtzite III-nitride nano-materials properties

Grégory Guisbiers,*[ab] Di Liu,[c] Qing Jiang*[c] and Lionel Buchaillot[a]

*Received 4th February 2010, Accepted 18th March 2010*
*First published as an Advance Article on the web 19th May 2010*
**DOI: 10.1039/c002496a**

In this paper, top-down and bottom-up approaches are used to predict material properties of group III-nitride nanostructures. The first approach calculates the melting temperature, melting enthalpy, Debye temperature and energy bandgap of InN, GaN and AlN through classical thermodynamics. The second approach calculates the surface energies in the liquid and solid states of the considered nitrides materials through molecular dynamics. Moreover, the liquid and solid surface energies of the zinc-blende and wurtzite III–V materials are compared. Finally, the phase diagram of a ternary III-nitride nanomaterial, AlGaN, is presented and the variation of its energy bandgap with composition is predicted.

## 1. Introduction

The III-nitride nanomaterials such as InN, GaN, AlN and their alloys represent an important group of semiconductors in optoelectronics.[1] This is primarily due to their direct bandgap that span a wide spectral range from infrared (IR) to ultraviolet (UV). The III-nitride materials have all a preferentially wurtzite crystal structure. Furthermore, AlN which is the only direct bandgap material in all Al containing III–V compounds, has also the largest energy bandgap of any material still commonly considered to be a semiconductor. In the III-nitride alloys, among the three ternary compounds InGaN, InAlN and AlGaN, the latter is the only one which is totally miscible in all the composition range.[2,3] AlGaN is used as a barrier material[1] for nitride electronic and optoelectronic devices and also as a UV photodetector material.[4] InGaN is a key constituent in blue diode lasers (DLs) and light emitting diodes (LEDs).[5] InAlN is a promising material for high efficiency solar cells.[6]

Due to the size and shape dependent materials properties such as the melting temperature, melting enthalpy, Debye temperature and energy bandgap, there is a strong interest to investigate these properties at the nanoscale for the III-nitride group. In this paper, we report a top-down approach coupled with a bottom-up approach to get the melting temperature, melting enthalpy, Debye temperature and energy bandgap of III-nitride nanomaterials. The bottom-up approach is used to predict the liquid and solid surface energies of InN, GaN and AlN. Moreover, the liquid and solid surface energies of zinc-blende and wurtzite III–V materials are compared. Finally, the phase diagram of AlGaN is plotted at the nanoscale as well as its energy bandgap *vs.* the alloy composition.

[a] *IEMN, CNRS-UMR8520, Scientific City, Avenue Henri Poincaré, BP 60069, 59652 Villeneuve d'Ascq, France. E-mail: gregory.guisbiers@physics.org*
[b] *Catholic University of Louvain (UCL), Institute of Mechanics, Materials and Civil Engineering, 2 Place Sainte Barbe, 1348 Louvain-la-Neuve, Belgium*
[c] *Key Laboratory of Automobile Materials (Jilin University), Ministry of Education, and School of Materials Sciences and Engineering, Jilin University, Changchun 130022, China. E-mail: Jiangq@jlu.edu.cn*

## 2. Theoretical determination of the melting temperature and melting enthalpy of III-nitride nanomaterials

Since the pioneering work of Pawlow[7] in 1909, many models describe the variation of the melting temperature with the particle size.[8] This behaviour is explained by the particular role played by the surface at the nanoscale.[9] Indeed when the size decreases, the number of atoms at the surface is no longer negligible compared to the number of atoms in the (bulk) volume. To study materials properties at the nanoscale, such as the melting temperature, there are two approaches currently used: top-down and bottom-up. The first makes use of classical thermodynamics whereas the second relies on computational methods such as molecular dynamics. Molecular dynamics, generally considers less than $10^6$ atoms, in order to keep calculation times within reasonable values.[10] This factor limits the nanostructure size modelled to a maximum size of around 100 nm,[11] on the other hand, effects such as chemical environment on the melting temperature can be considered. Within the top-down approach when dealing with nanostructures, care has to be taken with the validity of thermodynamics. Indeed, classical thermodynamics ceases to be valid when the thermal energy $kT$ becomes smaller than the energetic gap between two successive levels, $\delta$. According to Halperin,[12] when $\delta/k \sim 1$ K, the band energy splitting appears for a diameter $\sim$14 nm. When $\delta/k \sim 100$ K, this diameter becomes 3 nm in agreement with the value announced by Wautelet *et al.*[13] Therefore, these two methods are complementary.

Adopting the top-down approach using classical thermodynamics, we expressed the size and shape effects on melting temperature and melting enthalpy for free-standing nanostructures as function of the size of the structure and one shape parameter:[14]

$$\frac{T_m}{T_{m,\infty}} = 1 - \frac{\alpha_{shape}}{D} \quad (1)$$

$$\frac{\Delta H_m}{\Delta H_{m,\infty}} = 1 - \frac{\alpha_{shape}}{D} \quad (2)$$

Here $T_m$ (K) and $T_{m,\infty}$ (K) are the nanoscaled and bulk melting temperature, respectively; $\Delta H_m$ (J m$^{-3}$) and $\Delta H_{m,\infty}$ (J m$^{-3}$) are the nanoscaled and bulk melting enthalpy respectively; $D$ is the diameter of the structure and the shape parameter $\alpha_{shape}$ is defined as $\alpha_{shape} = AD(\gamma_s - \gamma_l)/(V\Delta H_{m,\infty})$; $A$ (m$^2$) and $V$ (m$^3$) are the surface area and volume of the nanostructure, respectively; $\gamma_l$ and $\gamma_s$ are the surface energy in the liquid and solid phases (J m$^{-2}$), respectively. The terms $\gamma_l$ and $\gamma_s$ are considered size independent. This is justified by the fact that the size effect on the surface energies are less than 4% for sizes higher than 4 nm.[16] These materials properties are indicated for III-nitride semiconductors in Table 1. The calculated shape parameters are indicated in Table 2.

For free-standing nanoparticles, the sphere has the lowest $\alpha_{shape}$ value. Let us note that $\alpha_{film}/\alpha_{sphere}$ and $\alpha_{wire}/\alpha_{sphere}$ equal 1/3 and 2/3, respectively, as already discussed by Wautelet.[15] In case of polyhedral nanoparticles, the higher the number of faces on the nanoparticle, the higher is the $\alpha_{shape}$ value. Therefore for a given size of nanoparticle, the nanoscaled melting temperature is higher for the sphere compared to the other shapes. This indicates a higher thermal stability for spherical free-standing nanoparticles due to Gibbs' energy minimization.[14]

**Table 1** Values of $\gamma_l$ and $\gamma_s$ for the GaN, InN and AlN crystals and the corresponding parameters for calculating them are also shown; $a$ is the lattice constant along the $x$ and $y$ axis, $c$ is the lattice constant along the $z$ axis. The bulk melting temperature, the bulk melting enthalpy, the bulk Debye temperature and the bulk energy bandgap are also indicated

| Properties/parameters | InN | GaN | AlN |
|---|---|---|---|
| Crystal structure[a] | Wurtzite | Wurtzite | Wurtzite |
| Molar mass/g mol$^{-1}$ | 128.8267 | 83.7267 | 40.9882 |
| $-E_{cb}{}^{g}$/eV atom$^{-1}$ | 3.75 | 4.56 | 5.83 |
| $-E_{cb\text{-}slab}{}^{g}$/eV atom$^{-1}$ | 3.72 | 4.52 | 5.80 |
| $a^g$/Å | 3.58 | 3.20 | 3.13 |
| $c^g$/Å | 5.78 | 5.18 | 5.02 |
| $T_{m,\infty}$/K | 2050[b] | 2570[b] | 3273[c] |
| $\Delta H_{m,\infty}$/J m$^{-3}$ | $3.13 \times 10^{9}$[d] | $9.74 \times 10^{9}$[d] | $1.63 \times 10^{10}$[g]<br>$8.75 \times 10^{9}$[c] |
| $T_{Debye,\infty}$/K | 660[e] | 600[d] | 950[e] |
| $E_{g,\infty}(T = 0$ K)/eV | 0.690[f] | 3.507[d] | 6.230[d] |
| $\gamma_l{}^{g}$/J m$^{-2}$ (eqn (5)) | | | |
| $T^* = 6000$ K | 0.93 | 1.42 | 2.43 |
| $T^* = 7000$ K | 0.87 | 1.45 | 2.2 |
| $T^* = 8000$ K | 0.81 | 1.51 | 2.24 |
| Average | 0.87 | 1.46 | 2.29 |
| $\gamma_l{}^{g}$/J m$^{-2}$ (eqn (6)) | 1.42 | 2.21 | 2.81 |
| $\gamma_l{}^{g}$/J m$^{-2}$ (eqn (7c)) | 1.24 | 1.72 | 2.33 |
| $N_s$ | 8 | | |
| $A_s$ | $(\sqrt{6}+\sqrt{2})a^2/4$ | | |
| Atomic site | 1st CN | 2nd CN | |
| $Z_{s1}$ | 3 | 9 | |
| $Z_{s2}$ | 4 | 9 | |
| $Z_b$ | 4 | 12 | |

[a] Ref. 1. [b] Ref. 26. [c] Ref. 27. [d] Ref. 41. [e] Ref. 42. [f] Ref. 51. [g] This work; $T^*$ is a 'pretreatment temperature'.

**Table 2** The shape parameters of the III-nitride semiconductors for a spherical nanoparticle, cylindrical nanowire and film

| | InN | GaN | AlN |
|---|---|---|---|
| $\alpha_{sphere}$/nm | 1.054 | 0.462 | 0.192 |
| $\alpha_{wire}$/nm | 0.702 | 0.308 | 0.128 |
| $\alpha_{film}$/nm | 0.351 | 0.154 | 0.064 |

## 3. Theoretical determination of the Debye temperature of III-nitride nanomaterials

Among materials properties, the Debye temperature, which is defined as in the Debye model of the specific heat as $T_{Debye,\infty} = \hbar\omega_{Debye,\infty}/k$, has received considerable attention since it is an essential physical quantity that determines the thermal transport properties. The Debye temperature is the temperature corresponding to the maximal energy which can excite lattice vibrations. According the Lindemann criterion of melting, the Debye temperature has a square-root dependence on the melting temperature.[17] Therefore, we have eqn (3) where $T_{Debye,\infty}$ is the bulk Debye temperature.

$$\frac{T_{Debye}}{T_{Debye,\infty}} = \sqrt{1 - \frac{\alpha_{shape}}{D}} \quad (3)$$

## 4. Theoretical determination of the energy bandgap of III-nitride nanomaterials

The energy bandgap is well known to be temperature dependent.[18] The energy bandgap of semiconductors increases when the temperature is decreased ($E_g = \Delta H_{cv} - T\Delta S_{cv}$). $\Delta H_{cv}$ and $\Delta S_{cv}$ represent the enthalpy and entropy variation between the conduction and valence electronic bands. This behaviour can be better understood if one considers that the interatomic spacing decreases when the amplitude of the atomic vibrations decreases due to the decreased thermal energy. A decreased interatomic spacing increases the potential seen by the electrons in the material, which in turn increases the size of the energy bandgap. Therefore such a temperature-dependent property is also size-dependent due to the size effect on the melting temperature (eqn (1)). Indeed, the melting temperature indicates the maximal temperature accessible by a solid nanostructure, therefore when $D$ decreases, the limit temperature $T$ decreases also ($T \propto 1 - \alpha_{shape}/D$) which increases $E_g$ ($E_g \propto -T$). Explicitly, using the Li equation:[19] $(E_g - E_{g,\infty})/E_{g,\infty} = 1 - T_m/T_{m,\infty}$, this means that with the same $\alpha_{shape}$ parameter, we can describe the size effect on the energy bandgap of semiconductors, $E_g$, with eqn (4) where $E_{g,\infty}$ is the bulk energy bandgap.[20]

$$\frac{E_g}{E_{g,\infty}} = 1 + \frac{\alpha_{shape}}{D} \quad (4)$$

## 5. Theoretical determination of the unknown surface energies of III-nitrides

From sections 2 and 3, it is clear that the surface plays a major role in nano/micro-technology, especially in the determination of the melting temperature, melting enthalpy, Debye temperature and energy bandgap of nanostructures. Therefore, it is important to evaluate the unknown surface energies of nitrides. First-principles density functional theory (DFT)[21] has been

performed using DMOL tools,[22] in which each electronic wave function was expanded in a localized atom-centered basis set. Each basis function was defined numerically on a dense radial grid, using a state-of-the-art delocalized internal coordinate optimization scheme. Generalized gradient approximation (GGA) with a Perdew–Burke–Ernzerholf (PBE) function[23] was employed as the exchange–correlation value. InN, GaN and AlN crystals have a wurtzite structure[24] and the corresponding lattice constants ($a$ and $c$) and cohesive energy ($E_{cb}$) are first calculated through optimizing the unit cell and are listed in Table 1. A $3 \times 3 \times 2$ superlattice with 72 atoms was built for all the three crystals, which is similar to those of GaAs and CdTe in the previous DFT simulation for liquid structures.[25] For this superlattice, the period lattice lengths in the three dimensions are about 10 Å, which are much larger than their corresponding nearest neighbor distance of about 2 Å. Thus, liquid structures in this superlattice were approximately valid since the size of the superlattice is large enough to neglect the interactions from outside the superlattice. To obtain the liquid structures, the dynamics calculation at fixed volume with a thermostat to maintain a constant temperature (NVT) was used. The constant temperature was set as 2500, 3000 and 3800 K separately for InN, GaN and AlN, which are just above the corresponding melting points of 2050, 2570 and 3273 K.[26,27] Usually, single crystals of group-III nitrides can not be grown from the liquid state under normal pressure conditions. For example, although high-quality bulk single crystals of GaN suitable for substrates are desired, the standard method of cooling its stoichiometric melt has been unsuccessful for GaN because it decomposes into Ga and $N_2$ at high temperatures before its melting point.[28] Through the high vapor pressure solution (adsorption high-pressure $N_2$ gas to Ga melt solution)[29] method, this problem can be solved and GaN single crystals are obtained. Similarly, according to the temperature–pressure ($T$–$P$) phase diagram of gallium nitride, with increasing $T$ to 1500–2500 K, GaN single crystals would decomposes to Ga and $N_2$ on the premise that $P < 6$ GPa,[28] which may also require solution techniques to obtain a liquid state. In our simulation, although it is difficult to introduce the solution environment, the NVT method can limit all the Ga and N atoms in the supercell, which play a similar role as solution for prohibiting GaN decomposition. It has been reported that the unit cell volume of solid GaN just before melting is almost equal to the initial value at ambient conditions.[28] Moreover, the Clausius–Clapeyron equation indicates that the volume change on melting or solidification of GaN must be very small because the slope of the temperature–pressure curve on melting is almost zero.[28] Thus, in this calculation, the fixed volume for GaN liquid structure $V_l$ is assumed to be equal to the corresponding bulk solid structure $V_s$. Since InN and AlN are similar to GaN both in geometric and electronic structures,[24] $V_l \approx V_s$ are also assumed for them, which may not lead to much error. For the first-principle dynamic simulation, the initial configurations of the three crystals were first heated at a temperature ($T$*) much higher than their melting points for 0.5 ps ($10^{-12}$ s). This "hot" temperature regime could eliminate any memory effect from the initial states.[25] Then, the dynamic simulations were fixed at the constant temperature mentioned above for 1 ps, which are comparable with those in the previous simulation.[25] The total number of dynamic steps is 500 and 1000 for the preheating and heating processes respectively; with a simulation time of 1 fs ($10^{-15}$ s) for each step. For the $\gamma_l$ calculation, since the surface area in our building supercell is $(3 \times 3)$, a small degree of randomness of surface species distribution and binding condition may induce a large deviation of calculated surface energy. For solving this problem, the preheating temperatures are respectively set as 6000, 7000 and 8000 K. These different preheating temperatures may bring different liquid surface structures and the average $\gamma_l$ values of them may eliminate the calculation error from randomness. The massive Nosé–Hoover method was chosen as the thermostat and the corresponding Nose Q ratio, Nose chain length and Yoshida parameter were respectively set as 2.0, 2 and 3. Using this method, the applied temperatures approached to the fixed ones after only 50 dynamic steps. The amplitude was smaller than 500 K after the temperature stabilization, which is small enough to avoid the applied temperatures being lower than the corresponding melting points. In the electronic aspect, the self consisting field (SCF) tolerance was set as $10^{-5}$ and the $k$-point was set as $2 \times 2 \times 2$. To reduce the computational cost, DFT Semi-core Pseudopots (DSPP)[30] is introduced through replacing the core electrons by a single effective potential including some degree of relativistic effects. Double numerical plus d-functions (DND) was chosen as the basis set with orbital cutoff of 4.2 Å. To speed up convergence, we used a smearing technique[31] and the smearing value is chosen as 0.005 Ha (1 Ha = 27.2114 eV).

After the preheating and heating processes for the three crystals, the periodic solid structures change to the disordered liquid ones, which are shown in Fig. 1. To confirm the simulated liquid structure, using the structure analysis in the Forcite tools, the radial distribution function (RDF) of GaN is shown in Fig. 2. It is found that except for the first neighbour peak, the RDF value $g(r)$ is quite broad and uniform, which confirms the formation of GaN liquid structure. InN and AlN show a similar situation to GaN. In addition, further dynamic optimization would not induce much change to the cohesive energy of these liquid structures, which could also prove that the simulation time is long enough and the liquid structures have reached energetic stability.

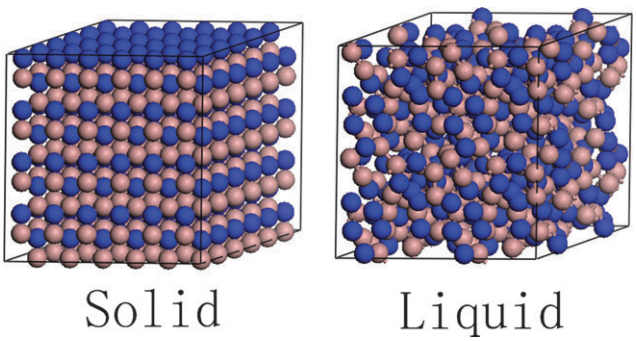


**Fig. 1** The illustration of the solid and liquid structures of wurtzite GaN, InN and AlN, where the pink atoms are Ga (or In, Al) and the blue atoms are N. The heating and preheating temperatures are shown in the text.

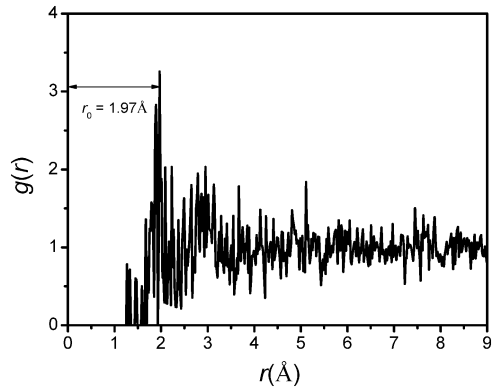


**Fig. 2** The radial distribution function (RDF) of the liquid structure of GaN, in which the first neighbor distance $r_0$ is shown.

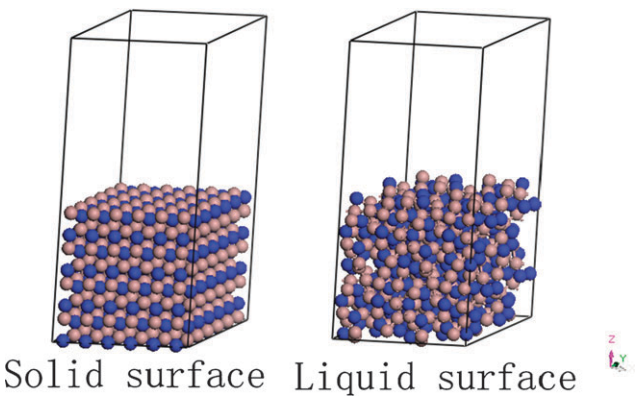


**Fig. 3** The illustration of the solid–vapor and liquid–vapor interface structure of the wurtzite GaN, InN and AlN, in which the $z$ axis (normal direction for both the solid–vapor and solid–liquid interfaces) is along [0001] and the crystal plane index for the solid–vapor interface or solid surface is (0001).

To calculate the liquid surface energy of the three crystals $\gamma_l$, two interfacial regions were created within the supercell of liquid structure through building a vacuum along the $z$ axis direction with vacuum distance of 12 Å,[32] which is far enough to forbid the interaction between them, and is shown in Fig. 3. The total interfacial area $A_i$ between the liquid and vapor phases is given as twice the cross-sectional area of the simulation cell $A_c$, namely $A_i = 2A_c = 2L_xL_y$ where $L_x$ and $L_y$ are the period lattice lengths of the supercell along the $x$ and $y$ axes; $\gamma_l$ is calculated by estimating the change of the Helmholtz free energy $F$ upon a change in $A_i$ as,[32] $\gamma_l = (\Delta F/\Delta A_i)_{N,V,T}$. Here $\Delta F = \Delta(U - TS) + \Delta E_{cs}$ where $U$, $T$ and $S$ are separately the internal energy, temperature and entropy; $\Delta E_{cs}$ is the cohesive energy increasing of the liquid surface atoms. Since $\Delta U = T\Delta S - P\Delta V$ ($P$ is the pressure and $V$ is the volume) and the simulation is under the condition of constant $T$ and $V$, $\Delta F = T\Delta S - P\Delta V - T\Delta S - S\Delta T + \Delta E_{cs} = \Delta E_{cs}$. Thus, $\gamma_l$ is deduced as,

$$\gamma_l = \left(\frac{\Delta E_{cs}}{\Delta A_i}\right)_{N,V,T} \quad (5)$$

For inorganic compounds with the wurtzite structure, the most probable surface of bulk solid is the (0001) crystal plane since it has the lowest Miller index, which brings the lowest solid surface energy $\gamma_s$. Thus, $\gamma_s$ of GaN, InN and AlN (0001) are investigated. The illustration of the wurtzite (0001) solid–vapor interface structure is also shown in Fig. 3. In DFT simulation, the solid surface energy of crystals has been determined as,[33] $\gamma_s = [(E_{c\text{-}slab}(N) - NE_{cb})/(2N_sA_s)]$ where $E_{c\text{-}slab}(N)$ is the cohesive energy of the slab with $N$ atoms, the factor "2" in the denominator indicates the two surfaces involved in the calculations due to three-dimensional boundary conditions, $N_s$ is the number of atoms at each surface and $A_s$ is the surface area occupied per atom. Although the interior atoms of the slab have no bond defects, their cohesive energy $E_{ci\text{-}slab}$ values are slightly larger than $E_{cb}$ since they are close to the surface. This cohesive energy difference may lead to errors for calculating $\gamma_s$. To avoid these errors, the "actual" bulk cohesive energy for the slab $E_{cb\text{-}slab}$ could be determined by the slope of the $E_{c\text{-}slab}(N)$ *vs.* $N$ function using the method proposed by Boettger.[34] Thus, $\gamma_s$ is revised as,

$$\gamma_s = \frac{E_{c\text{-}slab}(N) - NE_{cb\text{-}slab}}{2N_sA_s} \quad (6)$$

It has been reported that the five-layer slab is sufficient to describe the substrate of surface atoms since further increasing of slab thickness hardly changes its surface adsorption energy for a heterogeneous gas.[35] Based on this consideration, the $2 \times 2 \times (5/2)$, $2 \times 2 \times 3$, $2 \times 2 \times (7/2)$ (0001) slabs were separately built for geometric optimization, which are respectively five, six and seven layers of Ga (In, Al) and N atoms along the [0001]. The $N$ values for them are respectively 40, 48 and 56; $N_s$ and $A_s$ values are shown in Table 1. The $k$-point was set as $4 \times 4 \times 1$, which corresponds to the *medium* calculation quality level in the electronic setting of DFT simulation. The other settings for DFT simulation are the same as those for $\gamma_l$ calculation. After geometric optimization, inserting $E_{c\text{-}slab}(N)$ values of the three slabs into eqn (6), the $E_{c\text{-}slab}(N)$ *vs.* $N$ relationships are built and $E_{cb\text{-}slab}$ and $\gamma_s$ values are both obtained and indicated in Table 1.

In addition, $\gamma_s$ could also be evaluated based on the broken-bonds theory as,[36]

$$\gamma_s = \frac{-[2 - (Z_s/Z_b) - (Z_s/Z_b)^{1/2}]E_{cb}}{2A_s} \quad (7a)$$

where $Z_s$ and $Z_b$ are separately the coordinated number (CN) of surface and bulk atoms. For the inorganic elements or compounds, $\gamma_s$ is also related with the next-nearest neighbor CN as,[36]

$$\gamma_s = \frac{-\{[2 - (Z_s/Z_b) - (Z_s/Z_b)^{1/2}] + \beta[2 - (Z_s'/Z_b') - (Z_s'/Z_b')^{1/2}]\}E_{cb}}{(2 + 2\beta)A_s} \quad (7b)$$

where the superscript "′" denotes the next-nearest neighbor CN and $\beta$ shows the total bond strength ratio between the next-nearest and the nearest neighbors,[36] which is calculated as 3/10 for the wurtzite structure. Recently, this theoretical model was further developed for the high-Miller-index planes through considering the contribution of the subsurface atoms,

 

where $i$ denotes the $i$th layer of the surface.[37]

$$\gamma_s = -E_{cb}\sum_i \frac{\{[2-(Z_{s_i}/Z_b)-(Z_{s_i}/Z_b)^{1/2}]+\beta[2-(Z'_{s_i}/Z'_b)-(Z'_{s_i}/Z'_b)^{1/2}]\}}{(2+2\beta)A_s} \quad (7c)$$

Although the (0001) crystal plane has the lowest Miller index for the wurtzite structure, the revision in eqn (7c) is also suitable for it since its subsurface atoms still have next-nearest neighbor bonds defect, which is shown in Table 1. In eqn (7c), the $E_{cb}$ increasing in each surface atomic layer is considered and summed. Correspondingly, $A_s$ in Table 1 actually denotes the sum of surface area occupied per atom in each surface atomic layer. Based on eqn (7c), $\gamma_s$ values of GaN, InN and AlN are also calculated and shown in Table 1.

## 6. Discussion

In the DFT simulation, after the slabs are geometrically optimized, the bond lengths of surface atoms along the $z$ axis are much stretched, which may induce the $\gamma_s$ values further increasing. Since this factor can not be included in the theory calculation, $\gamma_s$ values by DFT simulation should be a bit larger than those by broken-bonds theory, which is in accord with the results in Table 1. For the liquid structures of group-III nitrides, it is found that $\gamma_l$ values for different preheating temperatures have only about 10% difference, which could prove the accuracy of our simulation. In the previous studies for the zinc-blende III–V materials[38] and metals,[39] the values of liquid surface energy $\gamma_l$ are all smaller than the corresponding $\gamma_s$ and the differences $\Delta\gamma = \gamma_s - \gamma_l$ are mostly in the range of 0.2–0.6 J m$^{-2}$.[38] In this article, it is found that $\gamma_l < \gamma_s$ is also valid for the nitrides with wurtzite structure. From DFT simulations, $\Delta\gamma$ for InN, GaN and AlN are equal to 0.55, 0.75 and 0.52 J m$^{-2}$, respectively. With the broken bonds theory, $\Delta\gamma$ values are 0.37, 0.26 and 0.04 J m$^{-2}$, which are smaller than the above values.

From the calculated surface energies, we can see that the surface energies of the III-nitride materials, in the liquid and solid states, evolve linearly with the molar mass.

$$\gamma_l = 2.90386 - 0.01614M \quad (8)$$

$$\gamma_s = 3.48537 - 0.01584M \quad (9)$$

A linear relation between surface energy and molar mass has also been shown in ref. 38 for phosphides, arsenides and antimonides III–V materials. Therefore, we can conclude that there exists a linear relationship between surface energies with molar mass for all III–V materials. This is illustrated in Fig. 4 where we can notice that the slope of the linear relation is different between wurtzite III–V materials from zinc-blende III–V materials; the slope is higher for wurtzite III–V materials than for zinc-blende ones. It means that for a similar molar mass, the surface energy is higher for III-nitride materials than for III-phosphide, arsenide or antimonide materials. This can be explained by the binding energy and the lattice constant. As mentioned above, GaN single crystals could be obtained through adsorption of high-pressure $N_2$ gas to a Ga melt solution.[29] Considering $N_2$ mixing with Ga (or In, Al) melt solutions, there is a large difference between the binding

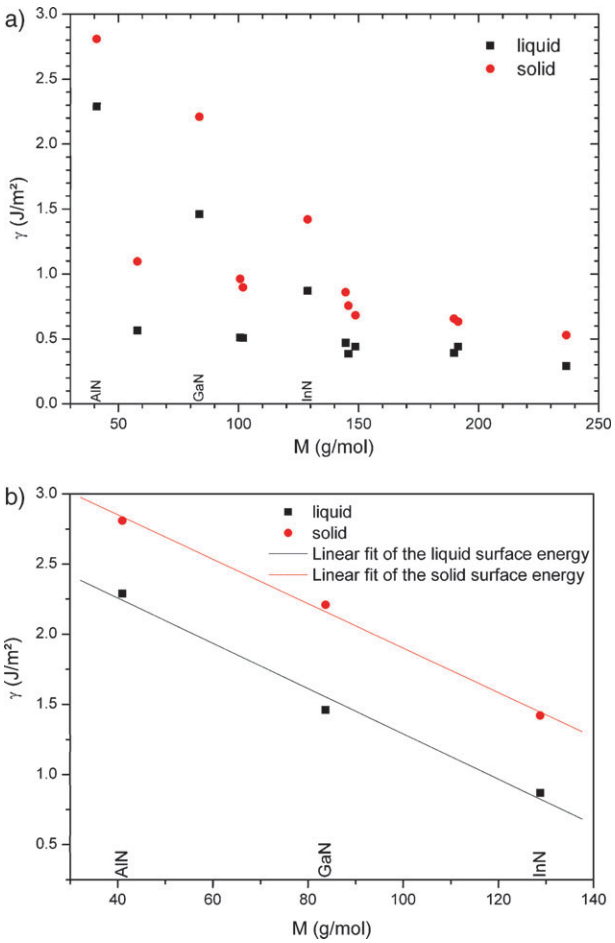


**Fig. 4** Surface energies in the liquid (black) and solid (red) states *vs.* the molar mass of the (a) III–V materials, (b) III-nitride materials only.

energy of the metal Al, In or Ga (~3 eV) and the $N_2$ molecule (~5 eV) making it preferable for the III-nitride system to have on the surface metallic atoms rather than N atoms.[40] For most other semiconductors, the binding energy is roughly the same for both components. Furthermore, the lattice constant of wurtzite III–V materials is smaller than those of the zinc-blende III–V materials.

With the values of the surface energies in hand, we can use eqn (1)–(4) to illustrate the size effect on melting temperature, melting enthalpy, Debye temperature and energy bandgap of InN, GaN and AlN. Fig. 5a–c show plots of the nanoscaled/bulk ratio of melting temperature, melting enthalpy and energy bandgap while Fig. 6 plots the nanoscaled/bulk ratio of the Debye temperature. For free-standing nanostructures, the melting temperature, melting enthalpy and Debye temperature decrease with size whereas the energy bandgap increases when the size is reduced.

Concerning the bulk melting enthalpy of AlN, the value taken from the Handbook of Martienssen–Warlimont[27] in Table 1 seems to be lower than the expected value because normally the melting enthalpy increases when the molar mass decreases. Based on the Landolt–Börnstein data,[41,42] the melting enthalpy of InN and GaN are known, however this is not the case with AlN. Therefore, we can extrapolate the

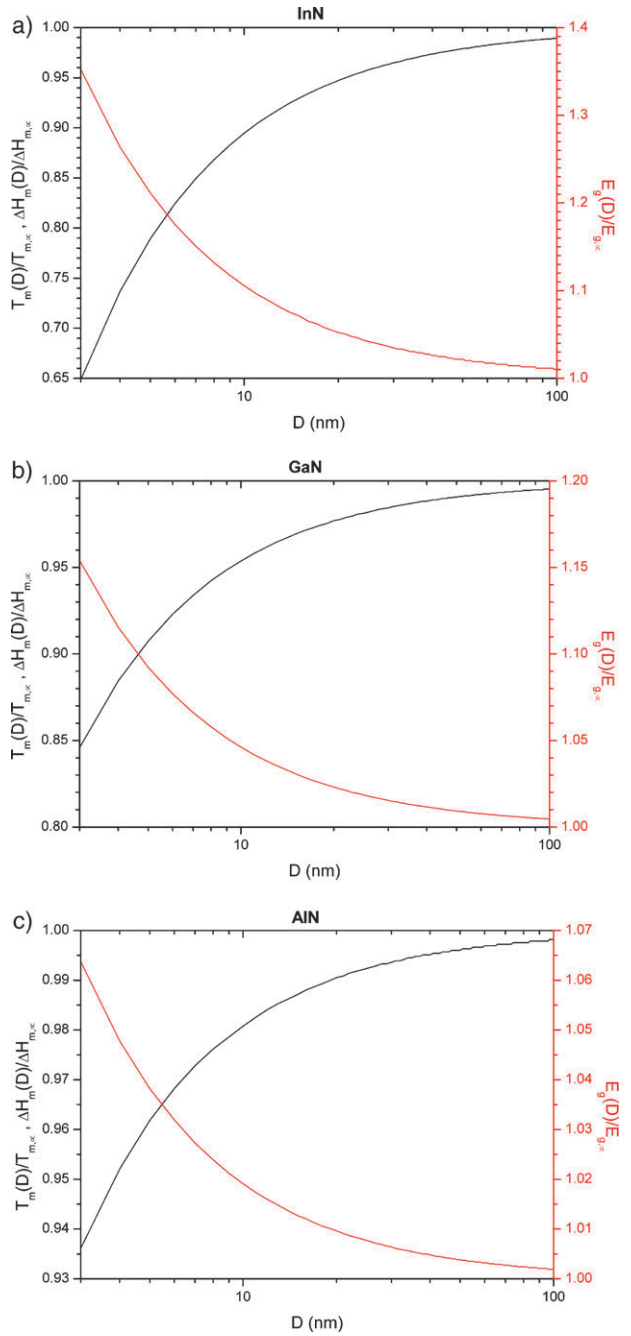


**Fig. 5** The nanoscaled/bulk melting temperature ratio, the nanoscaled/bulk melting enthalpy ratio and the nanoscaled/bulk energy bandgap ratio of (a) InN nanoparticles, (b) GaN nanoparticles and (c) AlN nanoparticles *vs.* diameter.

melting enthalpy of AlN through a linear fit of the melting enthalpy *vs.* the molar mass of the III-nitride compounds. A value of $1.63 \times 10^{10}$ J m$^{-3}$ has been found for AlN. It seems that particular attention has to be taken with the melting enthalpy of AlN as with its melting temperature due to its sensibility on pressure. Due to the linear relationship between the melting enthalpy and the molar mass, we note that the $\alpha_{shape}$ parameter decreases with the molar mass (Table 2) as also observed in ref. 38 with zinc-blende III–V materials. The $\alpha_{shape}$ values of AlN are lower than the values announced

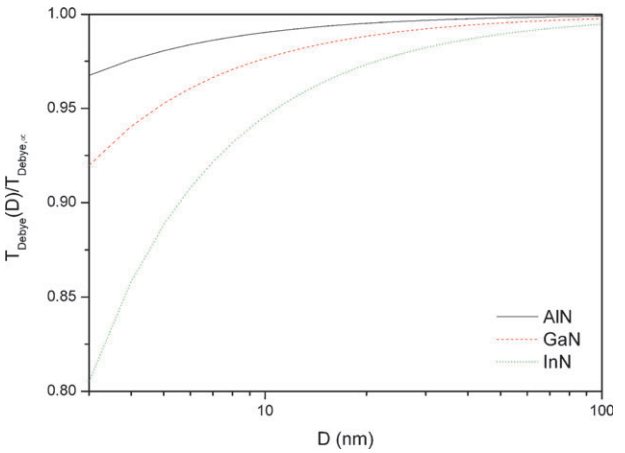


**Fig. 6** The nanoscaled/bulk Debye temperature ratio of InN, GaN and AlN spherical nanoparticles *vs.* diameter.

in ref. 43 where the calculation was done exclusively with Martienssen–Warlimont data. Here, the calculation is done with the simulated data announced in Table 1 for surface energies and the extrapolated data ($1.63 \times 10^{10}$ J m$^{-3}$) for the melting enthalpy.

## 7. Theoretical phase diagram of AlGaN

To our best knowledge, there are no papers discussing the size effect on the phase diagram of AlGaN semiconductor. According ref. 3 AlGaN is totally miscible; therefore, we can apply the assumption of ideal solutions. Considering no surface segregation, in the case of ideal solutions, the liquidus and solidus curves are calculated from the two simultaneous equations obtained by expressing the equality between the chemical potentials in the two phases.[44]

$$\begin{cases} kT\ln\left(\frac{x_{\text{solidus}}}{x_{\text{liquidus}}}\right) = \Delta H_{\text{m}}^{\text{A}}\left(1-\frac{T}{T_{\text{m}}^{\text{A}}}\right) \\ kT\ln\left(\frac{1-x_{\text{solidus}}}{1-x_{\text{liquidus}}}\right) = \Delta H_{\text{m}}^{\text{B}}\left(1-\frac{T}{T_{\text{m}}^{\text{B}}}\right) \end{cases} \quad (10)$$

Here $x_{\text{solidus}}$ ($x_{\text{liquidus}}$) is the composition in the solid (liquid) phase at a given $T$, respectively; $T_{\text{m}}^{i}$ is the melting temperature of the element $i$ and $\Delta H_{\text{m}}^{i}$ is the melting enthalpy of the element $i$.

The phase digram of AlGaN is plotted in Fig. 7 with solid lines and dashed lines, respectively, for the bulk and a non-segregated spherical nanoparticle with a diameter equal to 4 nm.

Let us now consider a possible surface segregation, it refers to the phenomenon by which the chemical composition at the surface of alloys differs from the composition in the core. Nanoalloys have the particularity to accommodate on the surface the structural defects introduced by the stoichiometric deviations. According to Williams and Nason,[45] the surface composition of the liquid and solid phase are given by:

$$\begin{cases} x_{\text{solidus}}^{\text{surface}} = \frac{(x_{\text{solidus}}/1-x_{\text{solidus}})\text{e}^{-(\Delta H_{\text{sub}} z_{1\text{v}})/(z_1 kT)}}{1+(x_{\text{solidus}}/1-x_{\text{solidus}})\text{e}^{-(\Delta H_{\text{sub}} z_{1\text{v}})/(z_1 kT)}} \\ x_{\text{liquidus}}^{\text{surface}} = \frac{(x_{\text{liquidus}}/1-x_{\text{liquidus}})\text{e}^{-(\Delta H_{\text{vap}} z_{1\text{v}})/(z_1 kT)}}{1+(x_{\text{liquidus}}/1-x_{\text{liquidus}})\text{e}^{-(\Delta H_{\text{vap}} z_{1\text{v}})/(z_1 kT)}} \end{cases} \quad (11)$$

Here $z_1$ is the first nearest neighbour atoms and $z_{1\text{v}}$ is the number of first nearest atoms above the same plane (vertical

 

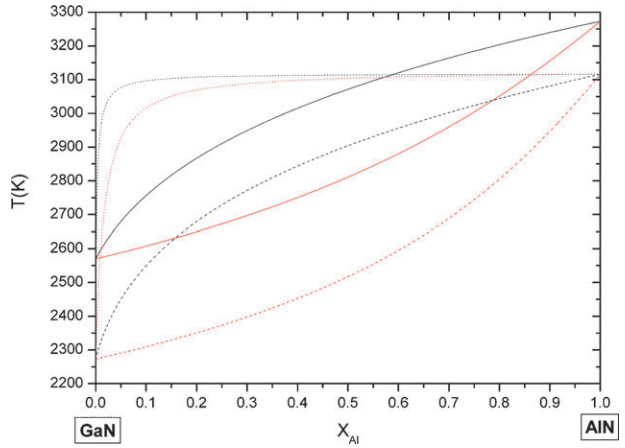


**Fig. 7** Phase diagram of AlGaN. The solidus (red) and liquidus (black) curves are indicated for the bulk material (solid lines) and the spherical nanomaterial (diameter = 4 nm) with (dotted lines) and without segregation (dashed lines).

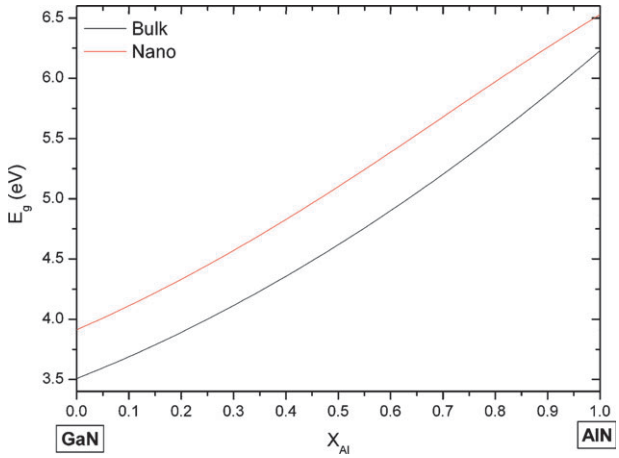


**Fig. 8** Direct energy bandgap of AlGaN *vs.* composition. The thick line indicates the bulk behavior and the thin one indicates the spherical nanomaterial behavior with a diameter equal to 4 nm and without segregation.

direction). In the case of the wurtzite crystal structure, we have $z_1 = 4$ and $z_{1v} = 1$; $\Delta H_{vap}$ is the difference between the vaporization enthalpies of the two pure elements, $\Delta H_{vap} = \Delta H_v^A - \Delta H_v^B$; $\Delta H_{sub}$ is the difference between the sublimation enthalpies of the two pure elements, $\Delta H_{sub} = \Delta H_s^A - \Delta H_s^B$. Element A is chosen to be the one with the highest sublimation and vaporization enthalpies. If the two components are identical, $\Delta H_{sub} = 0$ and $\Delta H_{vap} = 0$, there is no segregation and we retrieve eqn (10). The vaporization and sublimation enthalpies of GaN and AlN are unknown therefore we assume $\Delta H_{sub} = \Delta H_{vap} \approx 20kT$ to exhibit some segregation effect.[46] Looking at the phase diagram in Fig. 7, the solidus and liquidus curves of the segregated spherical nanoparticle are plotted with dotted lines. From it, we can deduce that the surface is enriched in gallium compared to aluminium producing a "core–shell" structure, in agreement with ref. 47. Furthermore, surface segregation promotes surface melting by placing at the surface the element with the lowest surface energy and then the lowest melting temperature. Indeed, it has been shown previously that melting temperature and surface energies evolve similarly with the atomic number.[48] In pure elements, the origin of surface melting is different and due to the bond breaking effect.[49]

## 8. Evolution of the AlGaN energy bandgap with composition

From the phase diagram, it is possible to deduce the variation of the energy bandgap of AlGaN nanomaterial *vs.* its composition. By a polynomial fit of the solidus curve, we can use the variation of the melting temperature with its composition to evaluate the variation of the $\alpha_{shape}$ parameter with the composition. Then with eqn (4) and (12), we can evaluate the variation of the energy bandgap of the nanostructure with its composition. Eqn (12) describes the energy bandgap behavior of the bulk as function of its composition.[50]

$$E_{g,\infty}(A_{1-x}B_x) = (1-x)E_{g,\infty}(A) + xE_{g,\infty}(B) - x(1-x)C \quad (12)$$

Here A and B represent the two binary compounds: AlN and GaN, $C$ is the bowing parameter of AlGaN which is equal to 1 eV,[50] and $x$ is the composition. The energy bandgap data is shown in Fig. 8 for AlGaN spherical nanomaterial.

## 9. Conclusions

To conclude, we have studied the size, shape, composition and segregation effects on the melting temperature, melting enthalpy, Debye temperature, energy bandgap and phase diagrams of miscible III-nitride semiconductors within a thermodynamical approach. The phase diagram of AlGaN was plotted for the first time at the nanoscale. Some deviation from our predictions is expected for sizes below the Bohr radius because quantum confinement has to be considered to be compared with optical measurements. Moreover, a careful experimental determination of the melting, vaporization and sublimation enthalpies is needed to fully apply eqn (10) and (11). A slight error in the determination of these values can be dramatic in the evaluation of the phase diagrams because these values are involved in the exponential factors of eqn (10) and (11). Finally, these thermodynamic considerations developed in this communication can assist to the tuning of the semiconductors optical properties.

## Acknowledgements

G. Guisbiers thanks the ANR PNANO project and the Belgian Federal Science Policy Office (BELSPO) through the "Mandats de retour" action for financial support. D. Liu and Q. Jiang thank National Key Basic Research and Development Program (Grant No. 2010CB631001) and by Program for Changjiang Scholars and Innovative Research Team in University.

## References

1 I. Vurgaftman and J. R. Meyer, *J. Appl. Phys.*, 2003, **94**, 3675.
2 I.-h. Ho and G. B. Stringfellow, *Appl. Phys. Lett.*, 1996, **69**, 2701.
3 V. G. Deibuk and A. V. Voznyi, *Semiconductors*, 2005, **39**, 623.

4 E. Muñoz, E. Monroy, J. L. Pau, F. Calle, F. Omnès and P. Gibart, *J. Phys.: Condens. Matter*, 2001, **13**, 7115.
5 S. Nakamura, T. Mukai and M. Senoh, *Appl. Phys. Lett.*, 1994, **64**, 1687; J. W. Orton and C. T. Foxon, *Rep. Prog. Phys.*, 1998, **61**, 1.
6 H. He, Y. Cao, R. Fu, W. Guo, Z. Huang, M. Wang, C. Huang, J. Huang and H. Wang, *Appl. Surf. Sci.*, 2010, **256**, 1812.
7 P. Pawlow, *Z. Phys. Chem.*, 1909, **65**, 1.
8 D. Ganguli, *Trans. Indian Ceram. Soc.*, 2008, **67**, 49.
9 Q. S. Mei and K. Lu, *Prog. Mater. Sci.*, 2007, **52**, 1175.
10 R. Holyst and M. Litniewski, *Phys. Rev. Lett.*, 2008, **100**, 055701.
11 W. H. Qi, *Phys. B*, 2005, **368**, 46.
12 W. P. Halperin, *Rev. Mod. Phys.*, 1986, **58**, 533.
13 M. Wautelet and D. Duvivier, *Eur. J. Phys.*, 2007, **28**, 953.
14 G. Guisbiers and L. Buchaillot, *J. Phys. Chem. C*, 2009, **113**, 3566.
15 M. Wautelet, *Phys. Lett. A*, 1998, **246**, 341.
16 L. H. Liang, M. Zhao and Q. Jiang, *J. Mater. Sci. Lett.*, 2002, **21**, 1843; R. C. Tolman, *J. Chem. Phys.*, 1949, **17**, 333; H. M. Lu and Q. Jiang, *J. Phys. Chem. B*, 2004, **108**, 5617; Z. Zhang, X. X. Lü and Q. Jiang, *Phys. B*, 1999, **270**, 249.
17 F. A. Lindemann, *Z. Phys.*, 1910, **11**, 609; M. X. Gu, C. Q. Sun, Z. Chen, T. C. Au Yeung, S. Li, C. M. Tan and V. Nosik, *Phys. Rev. B: Condens. Matter Mater. Phys.*, 2007, **75**, 125403; G. Guisbiers and L. Buchaillot, *Phys. Lett. A*, 2009, **374**, 305.
18 S. P. Keller, *Handbook on Semiconductors: Materials, Properties and Preparation (Volume 3)*, North-Holland Publishing Company, Amsterdam, 1980; J. A. Van Vechten and M. Wautelet, *Phys. Rev. B: Condens. Matter*, 1981, **23**, 5543.
19 M. Li and J. C. Li, *Mater. Lett.*, 2006, **60**, 2526.
20 G. Guisbiers, O. Van Overschelde and M. Wautelet, *Appl. Phys. Lett.*, 2008, **92**, 103121.
21 P. Hohenberg and W. Kohn, *Phys. Rev.*, 1964, **136**, B864; W. Kohn and L. J. Sham, *Phys. Rev.*, 1965, **140**, A1133.
22 B. Delley, *J. Chem. Phys.*, 1990, **92**, 508; B. Delley, *J. Chem. Phys.*, 2000, **113**, 7756.
23 J. P. Perdew, K. Burke and M. Ernzerhof, *Phys. Rev. Lett.*, 1996, **77**, 3865.
24 A. U. Scheleg and V. A. Sevastenko, *Vesti Akad. Nauk. BSSR Ser. Fiz. Mat. Nauk.*, 1976, **3**, 126; H. Schultz and K. H. Thiemann, *Solid State Commun.*, 1977, **23**, 815.
25 V. V. Godlevsky, J. J. Derby and J. R. Chelikowsky, *Phys. Rev. Lett.*, 1998, **81**, 4959.
26 V. P. Vasil'ev and J.-C. Gachon, *Inorg. Mater.*, 2006, **42**, 1176.
27 W. Martienssen and H. Warlimont, *Springer Handbook of Condensed Matter and Materials Data*, Springer, Berlin, 2005.
28 W. Utsumi, H. Saitoh, H. Kaneko, T. Watanuki, K. Aoki and O. Shimomura, *Nat. Mater.*, 2003, **2**, 735.
29 M. Bońkowski, I. Grzegory, S. Krukowski, B. Łucznik, Z. Romanowski, M. Wróblemski, J. Borysiuk, J. Weyher, P. Hageman and S. Porowski, *J. Cryst. Growth*, 2002, **246**, 194.
30 B. Delley, *Phys. Rev. B: Condens. Matter Mater. Phys.*, 2002, **66**, 155125.
31 J. M. Seminario and P. Politzer, *Theoretical and Computational Chemistry*, Elsevier Science, Amsterdam, 1995.
32 J. R. Errington and D. A. Kofke, *J. Chem. Phys.*, 2007, **127**, 174709.
33 W. Liu, W. T. Zheng and Q. Jiang, *Phys. Rev. B: Condens. Matter Mater. Phys.*, 2007, **75**, 235322.
34 J. C. Boettger, *Phys. Rev. B: Condens. Matter*, 1994, **49**, 16798.
35 S. Sakong, C. Mosch and A. Groß, *Phys. Chem. Chem. Phys.*, 2007, **9**, 2216.
36 Q. Jiang, H. M. Lu and M. Zhao, *J. Phys.: Condens. Matter*, 2004, **16**, 521.
37 J. Li, X. Luo, P. Hu and S. Dong, *J. Phys.: Condens. Matter*, 2009, **21**, 198001; D. Liu, H. M. Lu and Q. Jiang, *J. Phys.: Condens. Matter*, 2009, **21**, 198002.
38 G. Guisbiers, M. Wautelet and L. Buchaillot, *Phys. Rev. B: Condens. Matter Mater. Phys.*, 2009, **79**, 155426.
39 H. M. Lu and Q. Jiang, *J. Phys. Chem. B*, 2005, **109**, 15463.
40 J. Neugebauer, T. Zywietz, M. Scheffler and J. Northrup, *Appl. Surf. Sci.*, 2000, **159–160**, 355.
41 O. Madelung, *Landolt-Börnstein, Numerical data and functional relationships in science and technology, New series, Group III: Crystal and solid state physics, Semiconductors*, Springer-Verlag, Berlin, 1982.
42 O. Madelung, U. Rössler and M. Schulz, *Landolt-Börnstein, Numerical data and functional relationships in science and technology, Group III: Condensed Matter*, Springer-Verlag, Berlin, 2002.
43 G. Guisbiers and L. Buchaillot, *J. Phys. D: Appl. Phys.*, 2008, **41**, 172001.
44 G. Abudukelimu, G. Guisbiers and M. Wautelet, *J. Mater. Res.*, 2006, **21**, 2829; G. Guisbiers, G. Abudukelimu, F. Clement and M. Wautelet, *J. Comput. Theor. Nanosci.*, 2007, **4**, 309; R. Vallée, M. Wautelet, J. P. Dauchot and M. Hecq, *Nanotechnology*, 2001, **12**, 68.
45 F. L. Williams and D. Nason, *Surf. Sci.*, 1974, **45**, 377.
46 G. Guisbiers, G. Abudukelimu, M. Wautelet and L. Buchaillot, *J. Phys. Chem. C*, 2008, **112**, 17889.
47 P. Boguslawski, K. Rapcewicz and J. J. Bernholc, *Phys. Rev. B: Condens. Matter Mater. Phys.*, 2000, **61**, 10820.
48 G. Guisbiers, M. Kazan, O. Van Overschelde, M. Wautelet and S. Pereira, *J. Phys. Chem. C*, 2008, **112**, 4097.
49 C. Q. Sun, *Prog. Solid State Chem.*, 2007, **35**, 1.
50 I. Vurgaftman, J. R. Meyer and L. R. Ram-Mohan, *J. Appl. Phys.*, 2001, **89**, 5815.
51 J. Wu, W. Walukiewicz, K. M. Yu, J. W. I. Ager, E. E. Haller, H. Lu and W. J. Schaff, *Phys. Status Solidi B*, 2003, **240**, 412.


 